# Vacancy-related color centers in two-dimensional silicon carbide monolayers

M. Mohseni,[1, 2, 3] I. Abdolhosseini Sarsari,[3, *] S. Karbasizadeh,[3] Q. Hassanzada,[4] T. Ala-Nissila,[5, 6] and A. Gali[1, 7]

[1]*Wigner Research Centre for Physics, PO. Box 49, H-1525 Budapest, Hungary*
[2]*Loránd Eötvös University, Pázmány Péter Sétány 1/A, H-1117 Budapest, Hungary*
[3]*Department of Physics, Isfahan University of Technology, Isfahan, 84156-83111, Iran*
[4]*The NOMAD Laboratory at Fritz Haber Institute of the Max Planck*
*Society and IRIS Adlershof of the Humboldt University Berlin, Germany*
[5]*QTF Centre of Excellence, Department of Applied Physics, Aalto University, FI-00076 Aalto, Finland*
[6]*Interdisciplinary Center for Mathematical Modelling and Department of Mathematical Sciences,*
*Loughborough University, Loughborough, Leicestershire LE11 3TU, UK*
[7]*Department of Atomic Physics, Institute of Physics,*
*Budapest University of Technology and Economics,*
*Műegyetem rakpart 3., H-1111 Budapest, Hungary*
(Dated: August 22, 2022)

We examine vacancy defects in two-dimensional silicon carbide (2D-SiC) using density functional theory in order to explore their magneto-optical properties and their potential in quantum technologies. The defects include the silicon-vacancy ($V_{Si}$) and two antisite-vacancy pairs ($V_C$-$C_{Si}$ and $V_{Si}$-$C_{Si}$). We determine the characteristic hyperfine tensors and the fluorescence spectrum that are the key fingerprints of silicon-vacancy-related paramagnetic color centers in 2D-SiC and may be observed in electron paramagnetic resonance and photoluminescence experiments. In particular, we show that the $V_C$-$C_{Si}^-$ defect is promising candidate for a single-photon quantum emitter and qubit.

## I. INTRODUCTION

Point defects in semicondutors and related materials may significantly alter the host material's electrical, optical, and magnetic properties. In traditional semiconductors, shallow-level point defects may be used as dopants to deliberately introduce carriers. In contrast, deep-level point defects act as carrier traps or recombination centers that can deteriorate the operation of semiconductor devices. Recently, this negative view about deep-level point defects has been radically changed after a room-temperature electron spin resonance observation of a single point defect by optical means which was demonstrated on the negatively charged nitrogen-vacancy (NV) defect in diamond [1]. As the emission comes from a single defect, it can be considered to be a quantum or a single-photon emitter, which is required for quantum communication applications. The coherent manipulation and readout of a single spin is a realization of a quantum bit or qubit that can be employed in quantum sensing, simulation, computation, and entanglement-based quantum communication studies and applications [2, 3]. The success of the diamond-NV defect has motivated scientists to seek alternative paramagnetic quantum emitters which may have favorable magneto-optical or spin-coherence properties in technologically more mature materials than diamond. Since then, single-photon emitters with or without coherent manipulation of electron spins have been found in various materials, including the two dimensional (2D) ones [4]. The platforms offered by 2D materials have certain crucial advantages compared to the three dimensional (3D) bulk counterparts: they typically have very high extraction efficiency with avoiding total internal reflection and can be well integrated with cavities and photonic waveguides and coupled to plasmonic structures [5].

The first 2D material discovered [6], namely graphene, is a zero-band-gap material that cannot host single-photon emitters. Changing the chemical composition is one possible route to open the gap in carbon-based 2D materials. For instance, every second carbon atom may be replaced by a silicon atom to produce a 2D silicon–carbide (2D-SiC) honeycomb-structured material [7, 8]. This material should produce a band gap because of the partial polarization of the covalent bonds between the carbon and silicon and breaking the high symmetry of graphene. Very recently, the synthesis of this semiconductor material has been reported [9]. Although so far only a single study has reported the existence of this material it can nevertheless can be considered as an interesting platform with an $sp^2$ electronic configuration to host quantum emitters and qubits. In our previous study, our density-functional theory (DFT) calculations implied that 2D-SiC is a direct-wide-band-gap semiconductor in which preliminary results were achieved for some selected defects with a focus on, in particular, Stone-Wales related ones [10]. On the other hand, many color centers in 3D and 2D materials are vacancy-like and can be created either during growth or by irradiation techniques [4]. This motivates a detailed study of vacancy-type defects, especially silicon-vacancy related ones which have been reported to be candidates for qubits in 3D SiC [4, 11, 12].

The silicon-vacancy ($V_{Si}$) is simply a missing silicon atom in the SiC lattice (see Fig. 1). However, $V_{Si}$ has another atomic configuration when one of the neighboring carbon atoms jumps to the vacant site by creating a car-

bon antisite-vacancy pair, i.e., $V_C$-$C_{Si}$ (see Refs. 13–16). Finally, because the $C_{Si}$ defect has a very low formation energy in 2D-SiC [10], we also considered the complex of $V_{Si}$ and $C_{Si}$ defects, as shown in Fig. 1. The optical properties of $V_{Si}$ and $V_C$-$C_{Si}$ defects were studied previously in small systems [10] but a detailed magneto-optical characterization is still lacking for these important defects. Here we apply advanced plane-wave supercell density-functional theory (DFT) calculations to calculate the electronic structure, formation energies, photoionization thresholds, electron spin resonance hyperfine parameters, and basic optical parameters for these defects, and the fluorescence spectrum for the most relevant defect. Our results provide a reference for future electron spin resonance and photoluminescence studies of 2D-SiC. We find that the negatively charged $V_C$-$C_{Si}$ defect is a good candidate to function as a long-wavelength quantum emitter and can be used to realize a qubit in 2D-SiC.

## II. METHOD

In this work, we employ plane-wave supercell DFT calculations [17, 18] with the projector-augmented-wave (PAW) method [19, 20] as implemented in the Vienna Ab-initio Simulation Package (VASP) [21, 22]. The exchange-correlation functional of Heyd, Scuseria, and Ernzerhof [23] was used with its parameters set to standard values (HSE06). For all unit cell calculations, a dense Γ-centered $k$-point mesh of $9 \times 9 \times 1$ was used, while supercell calculations were performed using a single Γ point. The geometry was optimized with the criterion of $10^{-2}$ eV/Å per atom for the Hellman-Feynman forces and a kinetic energy cutoff of 450 eV was used. We employed a vacuum region of 12 Å and 24 Å in the $z$ direction for the $6 \times 6 \times 1$ and $8 \times 8 \times 1$ supercells, respectively, canceling all interactions between periodic images. The constrained DFT (CDFT) method [24] was implemented in VASP to calculate the electronically excited states, optimizing the geometry in these excited states.

For the calculation of phonon frequencies and normal coordinates, we used the same parameters as above for the vacuum region, cutoff energy, and $k$-point sampling. However, the more traditional functional of Perdew, Berke, and Ernzerhof (PBE) [25] was applied to optimize the forces on each atom within a threshold of $10^{-3}$ eV/Å. The phonons were calculated by DFT perturbation theory (DFPT) as implemented in VASP. Choosing the exchange-correlation functional of PBE over HSE06 in our phonon calculations provides reasonably accurate results while significantly reducing the computational time.

The fluorescence spectrum of the emitters may reveal their potential in various quantum technology applications. In quantum communication applications, the coherent emission only comes at the no-phonon or zero-phonon-line (ZPL) emission. The fraction of ZPL and

total emission can be observed in experiments and called the Debye-Waller factor ($W$). In the theoretical simulation of the emitters, Huang-Rhys (HR) theory may be applied to calculate the fluorescence spectrum's phonon sideband [26, 27]. The total Huang-Rhys factor ($S$) indicates in the HR theory that how many effective phonons participate in the optical transition and it is related to $W$ by

$$W = e^{-S}. \tag{1}$$

To calculate the phonon sideband of the spectrum, the partial HR factors should be calculated as explained in Ref. 26. The temperature dependent spectrum can be calculated by the Fourier-transform of the partial HR factor as

$$S(t) = \int_0^\infty S(\hbar\omega)F(\hbar\omega)e^{-i\omega t}d(\hbar\omega), \tag{2}$$

where $F(\hbar\omega)$ is the Bose-Einstein distribution function,

$$F(\hbar\omega) = \frac{1}{e^{\hbar w/k_B T} - 1}, \tag{3}$$

where $k_B$ is the Boltzmann-constant and $T$ is temperature. The phonon sideband of the spectrum can then be defined as

$$L(E_{ZPL} - \hbar\omega) = \frac{C\omega^3}{2\pi} \int_{-\infty}^\infty e^{[S(t)-S(0)]}e^{i\omega t - \gamma|t|}dt, \tag{4}$$

where $C$ is a normalization constant and $\gamma$ is the broadening of the ZPL emission. We use the Huang-Rhys theory to calculate the HR factors and the shape of the phonon sideband of the fluorescence spectrum.

## III. RESULTS

We investigate vacancy defects in a self-standing monolayer of 2D-SiC. We first briefly describe the host 2D-SiC system and then turn to the basic electronic structure of the vacancy defects. We present formation energies for the defects which reveal their relative stability, charge transition levels, and photoionization thresholds. We then determine the ground state spin properties of the paramagnetic vacancy defects. Finally, we compute and discuss their optical properties in detail by providing the fluorescence spectrum for the most relevant vacancy defects.

The pristine 2D-SiC crystal is optimized using HSE06 which yields a lattice constant of $a = 3.07$ Å and Si-C bond length of 1.77 Å, which agree well with the experimental data at 3.1 Å and 1.79 Å (see Ref. 9), respectively. The calculated band gap is 3.58 eV, which agrees well with our previous results and GW calculations [10, 28]. After optimizing the local 2D-SiC structure, we construct monolayer supercells, and embed the three vacancy defects considered here into them, as shown in Fig. 1.
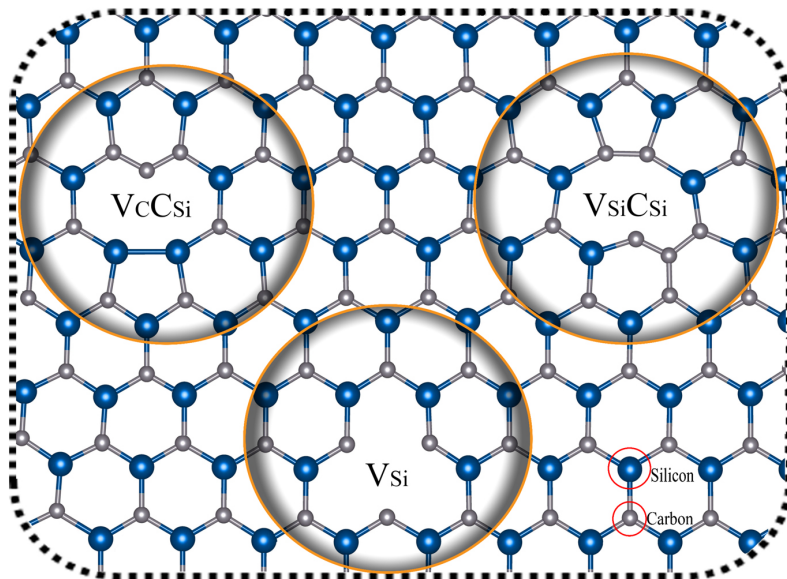
FIG. 1. Atomic structures of $V_{Si}$, $V_{Si}$-$C_{Si}$ and $V_C$-$C_{Si}$ defects after geometry optimization within $C_{2v}$, $C_s$ and $C_{2v}$ point group symmetries, respectively. Si and C atoms are represented by blue and grey spheres.
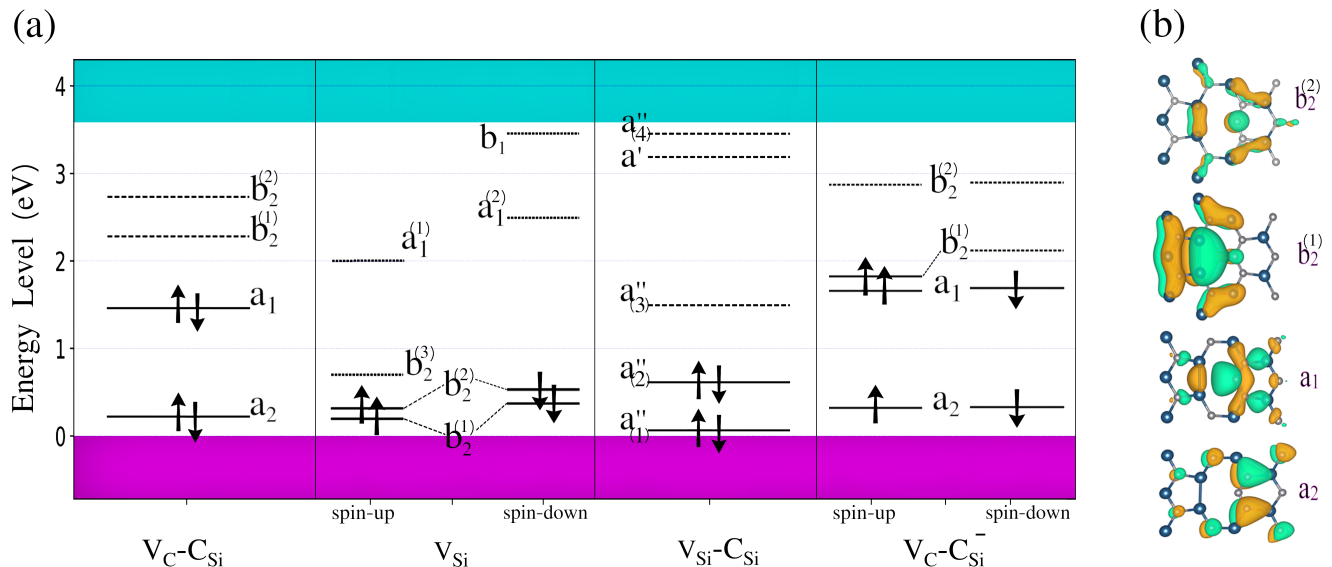


FIG. 2. Illustration of the electronic structure (a) in the ground state of $V_C$-$C_{Si}$, $V_{Si}$, $V_{Si}$-$C_{Si}$ and $V_C$-$C_{Si}^-$ defects (from left to right, respectively). Arrows show the spin direction of the electron. Each state is labeled according to the irreducible representation of the orbitals. Conduction band minimum (CBM) and valence band maximum (VBM) are shown with cyan and purple colors, respectively. (b) The corresponding Kohn-Sham wavefunctions of the electronic states of $V_C$-$C_{Si}^-$. Light green and brown lobes exhibit negative and positive isovalues. The isosurface absolute value is $10^{-8}$ Å$^{-3}$.

## A. Electronic structure of the vacancy defects

The neutral vacancy defects have dangling bonds that introduce occupied and empty defect levels in the fundamental band gap, depicted in Fig. 2 and labeled by the irreducible representation of the associated point group. We illustrate the symmetry of the Kohn-Sham wavefunctions on the $V_C$-$C_{Si}$ defect in Fig. 2(e) and the symmetries of the defects are indicated in Fig. 1. We note that the $V_{Si}$ defect is special in the sense, that it could have a high $D_{3h}$ symmetry generated by three dangling bonds. However, the spin-polarized DFT calculations show $C_{2v}$-symmetry electronic states. This is a signature of highly correlated electronic states for which the accuracy of the HSE06 functional may be worse than that for the other structures bearing single dangling bonds.

As a consequence of the filled and empty defect states in the gap, all the defects may be ionized by varying the position of the Fermi-level in the band gap. We thus consider positively and negatively charged defects in the

context as explained below.

## B. Formation energies, relative stability, charge transition levels, doping, and photoionization thresholds

The stability of the defect structures is determined via the formation energy. For a defect in charge state $q$, the formation energy ($E^F$) is given by [29],

$$E_q^F(\epsilon_F) = (E_q^{tot} + E_q^{corr}) - E_{perfect} - n_x \mu_x \quad (5)$$
$$+ q(\epsilon_{vbm}^{perfect} + \epsilon_F - \Delta V),$$

which depends on the Fermi-level energy $\epsilon_F$. The energies are referenced to the calculated valence band maximum (VBM) $\epsilon_{VBM}^{perfect}$. The quantities $E_q^{tot}$ and $E_q^{corr}$ are the total energy of the defected system and the finite-size electrostatic correction, respectively, both representing the charge state $q$. The term $E_{perfect}$ is the total energy of a pristine supercell of the same size, $n_x$ refers to the number of atoms of type $x$ added (positive) or removed (negative) from the perfect crystal, $\mu_x$ is the chemical potential of the newly added or removed atom, and $\Delta V$ is the alignment of the two electrostatic potentials of the pristine and defective supercells. The planar-averaged electrostatic potentials are obtained along the $z$ direction for both of the supercells, after which the difference $\Delta V$ between the values in a point far from the defect is considered.

The quantities $E_q^{corr}$ and $\Delta V$ were calculated using the software package CoFFEE [30] as

$$E_q^{corr} = E_q^{lat} - q\Delta V_{q-0/m}, \quad (6)$$

where $E_q^{lat} = E_q^{iso,m} - E_q^{per,m}$ is the long-range interaction energy which is obtained from solving the Poisson equation using a model charge distribution $\rho^m(r)$ and a model dielectric profile $V_q^{per,m}(r)$. $E_q^{per,m}$ is given by;

$$E_q^{per,m} = \frac{1}{2} \int_\Omega \rho^m(r) V_q^{per,m}(r) dr \quad (7)$$

where the integral is over the supercell volume, $\Omega$. $E_q^{per,m}$ is evaluated for larger supercells and extrapolated to obtain $E_q^{iso,m}$. $\Delta V_{q-0/m}$ gives the DFT difference electrostatic potential to the model potential as

$$\Delta V_{q-0/m} = (V_q^{DFT} - V_0^{DFT})|_{far} - V_q^{per,m}|_{far}. \quad (8)$$

When computing the formation energy, different growth conditions have to be taken into account. The relevant growth conditions for the 2D-SiC binary compound correspond to Si-rich and C-rich ones. When including these conditions into the formation energy, the chemical potential $\mu_x$ must be evaluated under such conditions. In the Si-rich case, $\mu_{Si}$ is calculated from a silicon crystal. The term $\mu_C$ is then taken from the equilibrium condition

$$\mu_{SiC} = \mu_{Si} + \mu_C, \quad (9)$$

where $\mu_{SiC}$ is the chemical potential of the 2D-SiC primitive cell. The same approach is used to determine $\mu_{Si}$ and $\mu_C$ in C-rich conditions. The formation energies of $V_C$-$C_{Si}$, $V_{Si}$-$C_{Si}$, and $V_{Si}$ are then computed using Eq. (5). The results are plotted in Fig. 3(a) for both Si-rich and C-rich conditions.

The $(+|0)$ charge transition levels for the defects in Fig. 3(a) fall well in the valence band. On the other hand, the $(0|-)$ charge transition level appears deep in the fundamental band gap at $\epsilon_{VBM}^{perfect} + 1.71$ eV, $\epsilon_{VBM}^{perfect} + 2.22$ eV and $\epsilon_{VBM}^{perfect} + 1.52$ eV for $V_C$-$C_{Si}$, $V_{Si}$ and $V_{Si}$-$C_{Si}$, respectively. We checked that the double-negative charge state is unstable, and the associated charge transition levels fall high in the conduction band.

We find that apart from under unrealistically extreme C-rich conditions, the $V_C$-$C_{Si}$ defect is the most stable among the vacancy defects considered here in 2D-SiC. Although $V_{Si}$ is stochiometric to $V_C$-$C_{Si}$, it can be considered a metastable form that we consider further in our study. Nevertheless, thermodynamic arguments imply that $V_C$-$C_{Si}$ will form at any position of the Fermi level. The $V_{Si}$-$C_{Si}$ defect is more stable than the isolated $V_{Si}$ defect.

In order to stabilize the acceptor states of the vacancy defects, donors should be introduced to 2D-SiC. It has been shown in SiC nanotubes [31] that nitrogen substituting carbon behaves as a donor. Using this idea, we considered nitrogen substituting carbon, $N_C$, as a donor candidate in 2D-SiC. In order to calculate its formation energy, the chemical potential of nitrogen should be known in Eq. (5). To this end, we considered the most stable structure of the hexagonal $Si_3N_4$ crystal with a $P6_3/m$ space group. Thus, the chemical potential of nitrogen ($\mu_N$) can be defined as

$$\mu_{Si_3N_4} = 3\mu_{Si} + 4\mu_N, \quad (10)$$

where $\mu_{Si_3N_4}$ is the chemical potential of the hexagonal $Si_3N_4$ primitive cell and $\mu_{Si}$ can vary between the Si-rich and C-rich conditions as set above. We find that the $N_C$ is indeed a donor in 2D-SiC with $(+|0)$ level at $\epsilon_{VBM}^{perfect} + 2.72$ eV or $\epsilon_{CBM}^{perfect} - 0.86$ eV (where CBM refers to conduction-band minimum) as shown in Fig. 3(b). The formation energy of $N_C$ is low; thus it is likely that $N_C$ doped 2D-SiC can support negatively charged vacancy defects in 2D-SiC.

Another way to realize a given charge state of the defect is by radiation. By applying a strong laser with energy above the ionization threshold, a defect can be driven to the photoionized charge state. Although photoionization may be harmful to realizing a stable emission from a given defect, photoionization threshold energies may be lower than the neutral excitation energies of the defect in a given charge state. The photoionization threshold energies of the vacancy defects can be read out in Fig. 3(a). We illustrate the role of photoionization on the most relevant $V_C$-$C_{Si}$ defect with $(0|-)$ level at $\epsilon_{VBM}^{perfect} + 1.71$ eV. Assuming that the defect was in
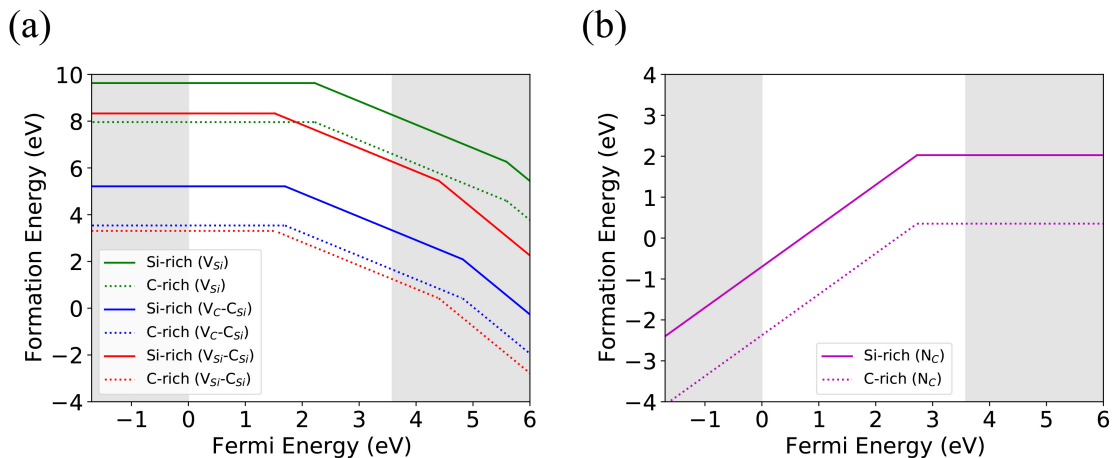
(a)

(b)



FIG. 3. Formation energy as a function of the Fermi level for (a) the vacancy defects $V_C$-$C_{Si}$, $V_{Si}$-$C_{Si}$ and $V_{Si}$, and (b) $N_C$ in Si-rich and C-rich growth conditions. The valence band maximum is aligned to zero, and the band regions are shown by shaded areas.

the neutral charge state, the illumination energy above 1.71 eV promotes an electron from the valence band to the empty defect level and drives the system to the negative charge state. On the other hand, assuming that the defect was in the negative charge state, an electron may be promoted from the occupied defect level to the conduction band by a $(3.58 - 1.71) = 1.87$ eV excitation energy. Thus, the condition of the existing fluorescence signal from the neutral and negatively charged $V_C$-$C_{Si}$ is that the associated optical excitation energies should be smaller than 1.71 eV and 1.87 eV, respectively. Using the same argument, these values are 2.22 eV and 1.36 eV for $V_{Si}$ and 1.52 eV and 2.06 eV for $V_{Si}$-$C_{Si}$, respectively.

## C. Hyperfine constants in the paramagnetic ground state of the defects

The neutral vacancy defects have a singlet ground state; however, the negatively-charged vacancy defects have a spin doublet ground state and they are spin-active paramagnetic defects. They can be in principle observed by electron paramagnetic resonance (EPR) methods. 2D-SiC consists of $^{13}$C and $^{29}$Si $I = 1/2$ nuclear spins with about 1.1% and 4.5% natural abundance; a hyperfine interaction is developed between the electron spin ($S = 1/2$) and the nuclear spins that are randomly distributed in the 2D-SiC crystal. For ensemble defect measurements, the statistics of the nuclear spin distribution proximate to the defect and the electron spin density distribution will produce a unique fingerprint in the associated EPR spectrum. Therefore, the EPR spectrum is a powerful method to identify the atomic structure of the defect, in particular, when combined with the DFT simulated spectra. The shape of the EPR spectrum of the $S = 1/2$ system is mostly set by the hyperfine (HF)

TABLE I. Computed hyperfine (HF) principal values ($A_{xx}$, $A_{yy}$ and $A_{zz}$) and their absolute average $[|A_{xx}| + |A_{yy}| + |A_{zz}|]/3$ in units of MHz for the nearest-neighbor atoms in the $V_C$-$C_{Si}^-$, $V_{Si}^-$ and $V_{Si}$-$C_{Si}^-$ defects. The atom labels are shown in Fig. 4. The values of the HF constants are given with core spin polarization. We note that the numerical accuracy of our data is about $\pm 0.3$ MHz.

| Defect | Atoms | $A_{xx}$ | $A_{yy}$ | $A_{zz}$ | Average |
|---|---|---|---|---|---|
| $V_C$-$C_{Si}^-$ | $C_1$ | $-2.9$ | $-7.3$ | $-1.7$ | 4.0 |
| | $C_2$-$C_3$ | $-5.5$ | $-3.9$ | $-5.9$ | 5.1 |
| | $C_4$-$C_5$ | $-5.5$ | $-3.5$ | $-6.2$ | 5.0 |
| | $Si_4$-$Si_5$ | $-4.3$ | $-3.9$ | $-15.7$ | 8.0 |
| | $Si_1$-$Si_2$ | 1.5 | 4.5 | $-101.3$ | 35.8 |
| | $Si_3$ | $-2.5$ | $-2.5$ | $-26.1$ | 10.4 |
| $V_{Si}^-$ | $C_1$-$C_2$ | 219.4 | 209.1 | 403.5 | 277.3 |
| | $C_3$ | $-194.1$ | $-182.8$ | $-368.8$ | 248.6 |
| $V_{Si}$-$C_{Si}^-$ | $C_1$ | 32.2 | 31.6 | 42.4 | 35.4 |
| | $C_2$ | 65.7 | 64.5 | 77.2 | 69.1 |
| | $C_3$ | 116.6 | 100.0 | 317.4 | 178.0 |
| | $C_4$ | $-25.0$ | $-19.4$ | $-38.3$ | 27.6 |
| | $C_5$ | 49.4 | 48.3 | 57.1 | 51.6 |
| | $C_6$ | 9.9 | 9.6 | 13.9 | 11.1 |

tensor for the nuclear spins which is given by

$$A_{ij} = \frac{1}{2S} \int d^3 r n_s(r) \gamma_I \gamma_e \hbar^2 [(\frac{8\pi}{3}\delta(r)) + (\frac{3x_i x_j}{r^5} - \frac{\delta_{ij}}{r^3})], \quad (11)$$
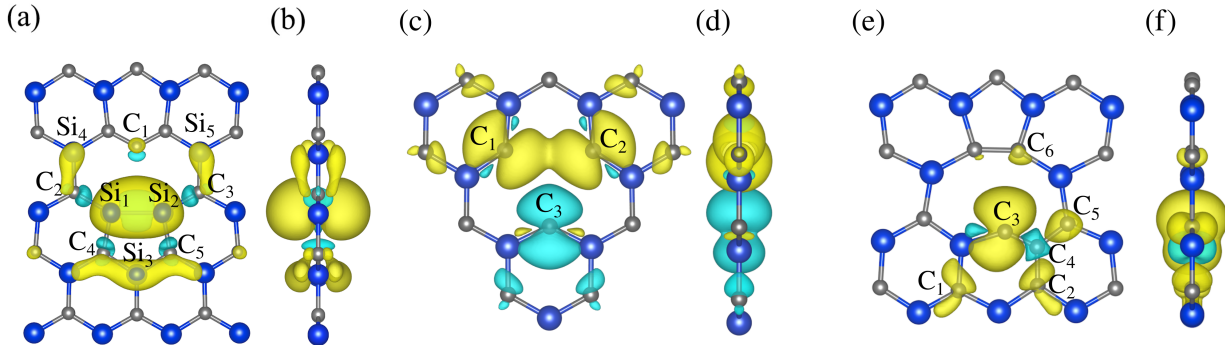
FIG. 4. Spin density of the (a) $V_C$-$C_{Si}^-$, (c) $V_{Si}^-$, and (e) $V_{Si}$-$C_{Si}^-$ defects from the top view and from the side in (b), (d) and (f), respectively. Si and C atoms are shown with blue and gray spheres, respectively. The hyperfine constants for the atoms labeled here are given in Table I. Light blue and yellow lobes exhibit negative and positive isovalues with respect to the average spin density, respectively. The isosurface absolute value is $10^{-3}$ Å$^{-3}$.

where $n_s(r)$ is the spin density of spin state $S$, $\gamma_e$ is the electron Bohr magneton and $\gamma_I$ is the nuclear Bohr magneton for nucleus $I$. The first and second terms in the parentheses represent the Fermi-contact and dipole-dipole terms, respectively. The dominance of the Fermi-contact term over the dipole-dipole one is well established as the Fermi-contact term strongly depends on the spin density localized at the nucleus. We note that Eq. (11) is modified within PAW formalism [32] as implemented by Martijn Marsman to the VASP code, and the spin-polarization of the core orbitals is taken into account for accurate HSE06 calculations [33]. The HF tensor can be diagonalized by yielding the three principal values, also known as the HF constants. The HF constants can be used to create a spin Hamiltonian that can be directly compared to the one from the experimental EPR spectrum. The HF constants are labeled $A_{xx}$, $A_{yy}$, and $A_{zz}$, following the convention that the largest absolute value is associated with $A_{zz}$.

Although the $V_{Si}^-$ defect is principally less stable than the other vacancy defects here, for the sake of completeness we computed the hyperfine tensors for all the three defects in their negative charge state for the immediate neighbor atoms of the defect as shown in Table I. The positions of the associated atoms and the spin density distribution are displayed in Fig. 4. In the $V_C$-$C_{Si}^-$ defect, the spin density is mainly localized on the $Si_1$ and $Si_2$ atoms, leading to an average HF constant of about 33 MHz. For $V_{Si}^-$, it is localized on $C_1$, $C_2$, and $C_3$ atoms with an average HF constant of 277 MHz for $C_1$-$C_2$ and 248 MHz for $C_3$. In $V_{Si}$-$C_{Si}^-$, the spin density is predominantly localized on a single carbon atom labeled as $C_3$; thus, the average HF constant is large, 178 MHz. We note that these defects produce very different EPR spectra and can be well identified by related measurements.

## D. Optical properties: zero-phonon-line and phonon sideband of the fluorescence spectrum, Debye-Waller factor and radiative lifetime

The vacancy defects introduce multiple filled and empty defect levels in the fundamental band gap in 2D-SiC. This may lead to visible or near-infrared emission upon photoexcitation below the photoionization threshold energies for the optically allowed transitions. Some of the excited states may have a zero optical transition dipole moment towards the electronic ground state by symmetry that we call dark states. The $V_{Si}$-$C_{Si}$ defect has a low $C_s$ symmetry with one symmetry plane; thus, all the excited states are principally optically allowed. The $V_C$-$C_{Si}$ and $V_{Si}$ defects have $C_{2v}$ symmetry, which may result in optically forbidden transitions between the $B_2$ and $B_1$ states, for instance.

In the neutral charge state of the vacancy defects, the closed-shell singlet ground state many-body wavefunction transforms as the trivial full symmetry irreducible representation, generally labeled as $A_1$ or $A'$ for $C_s$ symmetry. In the negative charge state of the vacancy defects, the ground state many-body wavefunction transforms as the unpaired electron Kohn-Sham states $B_2$, $A_1$, and $A''$ for $V_C$-$C_{Si}^-$, $V_{Si}^-$, and $V_{Si}$-$C_{Si}^-$ defects, respectively. The many-body wave functions of the excited states will transform as the product presentation of the unpaired electron Kohn-Sham states which are all irreducible for these particular cases.

We calculated the excited states with the CDFT method with full geometry optimization. The equilibrium geometry in the electronic ground and excited states may differ. Usually, the larger the difference the larger the phonon sideband in the fluorescence spectrum for the optically allowed transition. The difference in the geometries of the electronic ground and exited states ($\Delta Q$) may

be defined [34] as

$$\Delta Q^2 = \sum_{\alpha,i} m_\alpha (R_{\alpha,i}^{(e)} - R_{\alpha,i}^{(g)})^2, \qquad (12)$$

where $\alpha$ indicates the atom index, $i$ refers to the $x$, $y$ and $z$ coordinates, $m_\alpha$ is the atomic mass of species $\alpha$ and $R_{\alpha,i}^{(g/e)}$ is the position of atom $\alpha$ in the ground $(g)$/excited $(e)$ state. The calculated $\Delta Q$ values are listed for all possible transitions in Table II. Generally, these values are larger than 0.5 for most optically allowed transitions, which implies a large phonon sideband and a deficient Debye-Waller factor in the associated fluorescence spectra.

Based on the calculated relative stability and the $\Delta Q$ values for the vacancy defects in 2D-SiC, the most relevant configuration to realize single-photon emitters and qubits is the $V_C$-$C_{Si}$ defect in the neutral and negative charge states. Therefore, we restrict the detailed optical study to these defects.

In the neutral charge state, the two lowest-energy excited states have non-zero optical transition dipole moment separated by 0.77 eV (see Table III). We speculate that if the excitation energy is above the second excited state's energy, then the Kasha rule may break down because of the large energy gap between the second and first excited states, and emission is viable from the second excited state. Therefore, we provide the optical parameters for both excited states in Table III. In the negative charge state, the energy gap between the first and second excited states is only about 0.2 eV; thus, the Kasha rule is applied, and the phonons can rapidly cool the system from the second excited state to the lowest-energy excited state. Therefore, we provide the optical parameters only for the first excited state of $V_C$-$C_{Si}^-$.

The HR factors for the neutral defect are prominent $(> 8)$, which means a minor contribution from the coherent ZPL. We conclude that they are not applicable as quantum emitters for quantum communication applications. On the other hand, the $V_C$-$C_{Si}^-$ fluorescence spectrum displays a sharp ZPL emission even at room temperature (see Fig. 5). The calculated ZPL energy is at around 0.6 eV which falls in the infrared region. Although the emission wavelength is longer than the ultra-long wavelength region in commercial optical fibers, the transmission at the calculated ZPL wavelength is still effective in the optical fibers. Its radiative lifetime can be calculated [27, 35] as

$$\tau = \frac{n\omega^3 |\mu|^2}{3\pi\epsilon_0 \hbar c^3}, \qquad (13)$$

where $\mu$ is the optical transition dipole moment as calculated from the associated Kohn-Sham wavefunctions involved in the transition (cf. Tables II and III). In Eq. (13), $\hbar\omega$ is the excitation energy (ZPL energy in our case), $n$ is the refractive index, $c$ is the speed of light, and $\epsilon_0$ is the vacuum permittivity. The calculated value of $\mu$ is 8.48 Debye which results in $\tau = 155$ ns. The extraction

TABLE II. The calculated values of $\Delta Q$ (in units of Å amu$^{1/2}$) for the three different vacancy defects in 2D-SiC defects as obtained in a 72-atom supercell. The promotion of the electron from the occupied Kohn-Sham level to the empty Kohn-Sham level is shown in the first left column. The corresponding transition from the many-body ground state to the excited state by their symmetry is given in column 2 and column 4 for the defects (see also Fig. 2).

| El. conf. | Transition | $\Delta Q$ | Transition | $\Delta Q$ |
|---|---|---|---|---|
| | $V_C$-$C_{Si}$ | | $V_C$-$C_{Si}^-$ | |
| $a_1 - b_2^{(1)}$ | $A_1 - B_2^{(1)}$ | 1.17 | $B_2 - A_1^{(1)}$ | $0.87^a$ |
| $a_1 - b_2^{(2)}$ | $A_1 - B_2^{(2)}$ | $0.83^a$ | $B_2 - A_1^{(2)}$ | 0.39 |
| $a_2 - b_2^{(1)}$ | $A_1 - B_1^{(1)}$ | $0.85^a$ | $B_2 - A_2^{(1)}$ | $0.63^a$ |
| $a_2 - b_2^{(2)}$ | $A_1 - B_1^{(2)}$ | 0.37 | $B_2 - A_2^{(2)}$ | 1.09 |
| $b_2^{(1)} - b_2^{(2)}$ | - | - | $B_2^{(1)} - B_2^{(2)}$ | 0.46 |
| | $V_{Si}$ | | $V_{Si}^-$ | |
| $b_2^{(1)} - a_1^{(1)}$ | $A_1^{(1)} - B_2^{(1)}$ | 0.59 | $B_2^{(1)} - A_1^{(1)}$ | 1.81 |
| $b_2^{(1)} - a_1^{(2)}$ | $A_1^{(1)} - B_2^{(2)}$ | $0.94^a$ | $B_2^{(1)} - A_1^{(2)}$ | 0.80 |
| $b_2^{(2)} - a_1^{(1)}$ | $A_1^{(2)} - B_2^{(1)}$ | 1.48 | $B_2^{(2)} - A_1^{(1)}$ | $1.42^a$ |
| $b_2^{(2)} - a_1^{(2)}$ | $A_1^{(2)} - B_2^{(2)}$ | $1.03^a$ | $B_2^{(2)} - A_1^{(2)}$ | 1.1 |
| $b_2^{(3)} - a_1^{(1)}$ | - | - | $B_2^{(3)} - A_1^{(1)}$ | 1.09 |
| $b_2^{(3)} - a_1^{(2)}$ | - | - | $B_2^{(3)} - A_1^{(2)}$ | 0.91 |
| | $V_{Si}$-$C_{Si}$ | | $V_{Si}$-$C_{Si}^-$ | |
| $a''_{(1)} - a''_{(3)}$ | $A'_{(1)} - A'_{(3)}$ | 0.61 | $A''_{(1)} - A''_{(3)}$ | 0.96 |
| $a''_{(2)} - a''_{(3)}$ | $A'_{(2)} - A'_{(3)}$ | 0.78 | $A''_{(2)} - A''_{(3)}$ | 0.82 |
| $a''_{(1)} - a'$ | $A'_{(1)} - A''$ | 0.58 | $A''_{(1)} - A'$ | 0.87 |
| $a''_{(2)} - a'$ | $A'_{(2)} - A''$ | 0.53 | $A''_{(2)} - A'$ | 0.95 |
| $a''_{(3)} - a'$ | - | - | $A''_{(3)} - A'$ | 0.77 |
| $a''_{(3)} - a''_{(4)}$ | - | - | $A''_{(3)} - A''_{(4)}$ | 0.88 |

$a$ Data from Ref. [10]

of the emitted photon from a 2D material should be relatively efficient, therefore, the calculated optical lifetime implies that the fluorescence intensity would be sufficient to be observed at a single defect level.

## IV. SUMMARY AND CONCLUSIONS

Point defects and vacancies in particular in semiconducting materials are promising candidates as coherent single-photon emitters and qubits in quantum technology applications. In this work we have studied some of the

TABLE III. Calculated zero-phonon-line energy (ZPL), ZPL wavelength ($\lambda$), Huang-Rhys factor (HR) and Debye-Waller factor (DW) factor for the $V_C$-$C_{Si}$ defect in the neutral and negative charge states as obtained in the 128-atom supercell. The two lowest-energy excited state solutions are shown for the neutral $V_C$-$C_{Si}$.

| Defect | Transition | $E_{ZPL}$ (eV) | $\lambda_{ZPL}$ (nm) | HR | DW (%) |
|---|---|---|---|---|---|
| $V_C$-$C_{Si}$ | $A_1 - B_2^{(1)}$ | 0.50 | 2479 | 8.8 | 0.01% |
| | $A_1 - B_2^{(2)}$ | 1.27 | 976 | 9.41 | 0.008% |
| $V_C$-$C_{Si}^-$ | $B_2^{(1)} - B_2^{(2)}$ | 0.59 | 2101 | 0.80 | 44% |
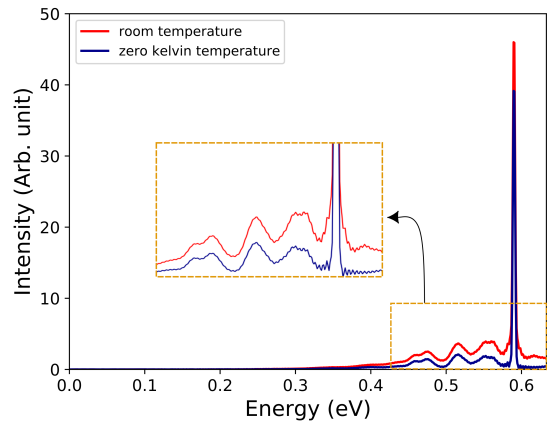


FIG. 5. Simulated fluorescence spectrum for the $B_2^{(1)} - B_2^{(2)}$ transition of the $V_C$-$C_{Si}^-$ defect at different temperatures.

most promising silicon-vacancy-related defects in 2D-SiC through plane-wave supercell DFT calculations. The $V_C$-$C_{Si}$ defect is the most stable among the defect types that we considered, providing paramagnetic and fluorescent signals in the negative charge state. We found that this acceptor state may be realized in nitrogen-donor-doped 2D-SiC material. Since the other defects might also form with irradiation techniques, we provided their hyperfine coupling parameters in the negative charge state as fingerprints in their EPR spectrum. The optical properties of the most stable $V_C$-$C_{Si}^-$ defect were characterized in detail. We found a favorable Debye-Waller factor (44%) and a relatively short optical lifetime (155 ns) which makes this defect a good candidate to be considered as a single photon emitter in 2D-SiC.

## ACKNOWLEDGMENTS

[1] A. Gruber, A. Dräbenstedt, C. Tietz, L. Fleury, J. Wrachtrup, and C. v. Borczyskowski, Science **276**, 2012 (1997).

[2] M. W. Doherty, N. B. Manson, P. Delaney, F. Jelezko, J. Wrachtrup, and L. C. L. Hollenberg, Physics Reports The nitrogen-vacancy colour centre in diamond, **528**, 1 (2013).

[3] A. Gali, Nanophotonics **8**, 1907 (2019).

[4] G. Zhang, Y. Cheng, J.-P. Chou, and A. Gali, Applied Physics Reviews **7**, 031308 (2020), publisher: American Institute of Physics.

[5] I. Aharonovich, D. Englund, and M. Toth, Nature Photonics **10**, 631 (2016).

[6] K. S. Novoselov, A. K. Geim, S. V. Morozov, D. Jiang, Y. Zhang, S. V. Dubonos, I. V. Grigorieva, and A. A. Firsov, Science **306**, 666 (2004).

[7] S. Lin, S. Zhang, X. Li, W. Xu, X. Pi, X. Liu, F. Wang, H. Wu, and H. Chen, The Journal of Physical Chemistry C **119**, 19772 (2015).

[8] T. Susi, V. Skákalová, A. Mittelberger, P. Kotrusz, M. Hulman, T. J. Pennycook, C. Mangler, J. Kotakoski, and J. C. Meyer, Scientific Reports **7**, 4399 (2017).

[9] S. Chabi, Z. Guler, A. J. Brearley, A. D. Benavidez, and T. S. Luk, Nanomaterials **11** (2021), 10.3390/nano11071799.

[10] Q. Hassanzada, I. A. Sarsari, A. Hashemi, A. Ghojavand, A. Gali, and M. Abdi, Phys. Rev. B **102**, 134103 (2020).

[11] D. Riedel, F. Fuchs, H. Kraus, S. Väth, A. Sperlich, V. Dyakonov, A. A. Soltamova, P. G. Baranov, V. A. Ilyin, and G. V. Astakhov, Physical Review Letters **109**, 226402 (2012).

[12] M. Widmann, S.-Y. Lee, T. Rendler, N. T. Son, H. Fedder, S. Paik, L.-P. Yang, N. Zhao, S. Yang, I. Booker, A. Denisenko, M. Jamali, S. A. Momenzadeh, I. Gerhardt, T. Ohshima, A. Gali, E. Janzén, and J. Wrachtrup, Nature Materials **14**, 164 (2015).

[13] E. Rauls, T. Lingner, Z. Hajnal, S. Greulich-Weber, T. Frauenheim, and J.-M. Spaeth, physica status solidi (b) **217**, r1 (2000).

[14] T. Umeda, J. Ishoya, T. Ohshima, N. Morishita, H. Itoh, and A. Gali, Phys. Rev. B **75**, 245202 (2007).

[15] S. Castelletto, B. C. Johnson, V. Ivády, N. Stavrias, T. Umeda, A. Gali, and T. Ohshima, Nature Materials **13**, 151 (2014).

[16] S. Castelletto, B. C. Johnson, C. Zachreson, D. Beke, I. Balogh, T. Ohshima, I. Aharonovich, and A. Gali, ACS Nano **8**, 7938 (2014).

[17] W. Kohn and L. J. Sham, Phys. Rev. **140**, A1133 (1965).

[18] P. Hohenberg and W. Kohn, Phys. Rev. **136**, B864 (1964).

[19] P. E. Blöchl, Phys. Rev. B **50**, 17953 (1994).

[20] G. Kresse and D. Joubert, Phys. Rev. B **59**, 1758 (1999).

[21] G. Kresse and J. Furthmüller, Phys. Rev. B **54**, 11169 (1996).

[22] G. Kresse and J. Furthmüller, Computational Materials Science **6**, 15 (1996).

[23] J. Heyd, G. E. Scuseria, and M. Ernzerhof, The Journal of Chemical Physics **118**, 8207 (2003).

[24] A. Gali, E. Janzén, P. Deák, G. Kresse, and E. Kaxiras, Phys. Rev. Lett. **103**, 186404 (2009).

[25] J. P. Perdew, K. Burke, and M. Ernzerhof, Phys. Rev. Lett. **77**, 3865 (1996).

[26] A. Alkauskas, B. B. Buckley, D. D. Awschalom, and C. G. V. de Walle, New Journal of Physics **16**, 073026 (2014).

[27] G. Thiering and A. Gali, Physical Review X **8** (2018), 10.1103/PhysRevX.8.021063.

[28] H. C. Hsueh, G. Y. Guo, and S. G. Louie, Phys. Rev. B **84**, 085404 (2011).

[29] H.-P. Komsa, T. T. Rantala, and A. Pasquarello, Phys. Rev. B **86**, 045112 (2012).

[30] M. H. Naik and M. Jain, Computer Physics Communications **226**, 114 (2018).

[31] A. Gali, Phys. Rev. B **73**, 245415 (2006).

[32] Z. Bodrog and A. Gali, Journal of Physics: Condensed Matter **26**, 015305 (2014).

[33] K. Szász, T. Hornos, M. Marsman, and A. Gali, Phys. Rev. B **88**, 075202 (2013).

[34] A. Alkauskas, J. L. Lyons, D. Steiauf, and C. G. Van de Walle, Phys. Rev. Lett. **109**, 267401 (2012).

[35] V. Weisskopf and E. Wigner, Zeitschrift für Physik **63**, 54 (1930).